Chapter 3
Experimental Nonlinear Dynamics and Snap-Through of Post-Buckled Composite Plates

H.-G. Kim and R. Wiebe

Abstract Modern aerospace systems are beginning to see the use of composite panels and plates to achieve light weight and specific strength and stiffness. For constrained panels, thermally-induced axial loading may cause buckling of the structure, which can lead to nonlinear and potentially chaotic behavior. When post-buckled composite plates experience snap-through, they are subjected to large-amplitude deformations and in-plane compressive loading. These phenomena pose a potential threat to the structural integrity of composite structures. In this work, the nonlinear dynamics of post-buckled composite plates are investigated. In the experiment, an electrodynamic shaker is used to directly control the harmonic loads and the digital image correlation (DIC) technique is used to capture the dynamic response. Both chaotic (intermittent) and periodic (persistent) steady-state snap-through behaviors are investigated. The experimental results are compared to numerical analysis from a theoretical model based on the classical laminated plate theory (CLPT) using the von Karman strain-displacement relations.

Keywords Nonlinear dynamics • Snap-through • Experimental mechanics • Composite plates • Post-buckled plates

3.1 Introduction

The industrial application of composite materials has grown significantly during the last half century due to its high strength and low density [1]. The Boeing 787, which is the first commercial airliner with a composite fuselage and wings, is a compelling example of the structural application of composite materials. Fifty percent of its primary structures, including the fuselage and wings, is made up of carbon fiber/epoxy composite materials, or carbon fiber-reinforced plastics (CFRP) [2]. For constrained panels, thermally-induced axial loading such as aerodynamic heating during flight may cause buckling [3, 4], which can lead to nonlinear and potentially chaotic behavior, including snap-through of post-buckled panels between their stable equilibria. When post-buckled composite plates experience snap-through, they are subjected to large-amplitude deformations and significant in-plane compressive loading. These phenomena pose a potential threat to the structural integrity of composite structures; for example, axial compression may accelerate delamination growth which can lead to loss of global stability [5]. Delamination, which appears as a debonding of adjacent layers in laminated composites, is a very important failure mode in composite laminates [2] and one of the most frequently occurring failures of laminated composite structures [6]. In addition, snap-through makes abrupt curvature changes, which possibly leads to a considerable decrease in fatigue life [7, 8]. Therefore, understanding the post-buckled behavior of composite structure is pivotal to the safety of these structures.

The primary focus of this work is the characterization of dynamic snap-through of post-buckled thin laminated composite plates under harmonic loads. Snap-through behaviors can be categorized as chaotic (intermittent) and periodic (persistent) snap-through [7, 8]. When a post-buckled plate is subjected to a relatively small amplitude dynamic loading, the plate oscillates around one of its stable equilibria (i.e., a single-well response). As the forcing amplitude increases, the plate begins to show chaotic snap-through behaviors and with a further increase in the load, the response shifts to periodic snap-through. The first and second thresholds are labeled chaotic and periodic snap-through boundaries, respectively. These behaviors are experimentally and numerically investigated.

In the experiment, the dynamic response of a post-buckled plate specimen was collected using the digital image correlation (DIC) technique, which provides a full-field displacement measurement. The post-buckled behavior is modeled based on the classical laminated plate theory (CLPT) using the von Kármán strain-displacement relations. The arc-length method

H.-G. Kim (✉) • R. Wiebe
Department of Civil and Environmental Engineering, University of Washington, Seattle, WA 98195, USA
e-mail: hgyukim@uw.edu

© The Society for Experimental Mechanics, Inc. 2017

G. Kerschen (ed.), *Nonlinear Dynamics, Volume 1*, Conference Proceedings of the Society for Experimental Mechanics Series, DOI 10.1007/978-3-319-54404-5_3

with a branch switching technique at bifurcation points is used to find the static equilibrium path of the post-buckled plate specimen. The Newmark-beta method with the Newton-Raphson method is adopted to model nonlinear dynamic response of the specimen. The numerical analysis results from the model are compared with the experimental data.

3.2 Theoretical Nonlinear Model for Post-Buckled Plates

In this paper, the classical laminated plate theory (CLPT) is used to establish the theoretical model. The derivation of the nonlinear equation of motion of CLPT is well explained in many books such as [9] and [10]. In this section, nonlinear equations of motion in Eq. (3.1) are presented based on the Reddy's work in [9].

$$
\begin{aligned}
&-\left(\frac{\partial N_{xx}}{\partial x}+\frac{\partial N_{xy}}{\partial y}\right)+\rho_0 h\frac{\partial^2 u_0}{\partial t^2}=0\\
&-\left(\frac{\partial N_{xy}}{\partial x}+\frac{\partial N_{yy}}{\partial y}\right)+\rho_0 h\frac{\partial^2 v_0}{\partial t^2}=0\\
&-\left(\frac{\partial^2 M_{xx}}{\partial x^2}+2\frac{\partial^2 M_{xy}}{\partial y\partial x}+\frac{\partial^2 M_{yy}}{\partial^2 y}\right)-\frac{\partial}{\partial x}\left(N_{xx}\frac{\partial w_0}{\partial x}+N_{xy}\frac{\partial w_0}{\partial y}\right)-\frac{\partial}{\partial y}\left(N_{xy}\frac{\partial w_0}{\partial x}+N_{yy}\frac{\partial w_0}{\partial y}\right)-q\\
&+\rho h\frac{\partial^2 w_0}{\partial t^2}-\frac{\rho_0 h^3}{12}\frac{\partial^2}{\partial t^2}\left(\frac{\partial^2 w_0}{\partial x^2}+\frac{\partial^2 w_0}{\partial y^2}\right)=0
\end{aligned}
\tag{3.1}
$$

where N_{xx}, N_{yy}, and N_{xy} are in-plane force resultants, and M_{xx}, M_{yy}, and M_{xy} are moment resultants given in Eq. (3.2).

$$
\begin{aligned}
\begin{Bmatrix} N_{xx}\\ N_{yy}\\ N_{xy}\end{Bmatrix} &= \begin{bmatrix} A_{11} & A_{12} & A_{16}\\ A_{12} & A_{22} & A_{26}\\ A_{16} & A_{26} & A_{66}\end{bmatrix}\begin{Bmatrix} \frac{\partial u_0}{\partial x}+\frac{1}{2}\left(\frac{\partial w_0}{\partial x}\right)^2\\ \frac{\partial v_0}{\partial y}+\frac{1}{2}\left(\frac{\partial w_0}{\partial y}\right)^2\\ \frac{\partial u_0}{\partial y}+\frac{\partial v_0}{\partial x}+\frac{\partial w_0}{\partial x}\frac{\partial w_0}{\partial y}\end{Bmatrix}+\begin{bmatrix} B_{11} & B_{12} & B_{16}\\ B_{12} & B_{22} & B_{26}\\ B_{16} & B_{26} & B_{66}\end{bmatrix}\begin{Bmatrix} -\frac{\partial^2 w_0}{\partial x^2}\\ -\frac{\partial^2 w_0}{\partial y^2}\\ -2\frac{\partial^2 w_0}{\partial x\partial y}\end{Bmatrix}\\
\begin{Bmatrix} M_{xx}\\ M_{yy}\\ M_{xy}\end{Bmatrix} &= \begin{bmatrix} B_{11} & B_{12} & B_{16}\\ B_{12} & A_{22} & B_{26}\\ B_{16} & B_{26} & B_{66}\end{bmatrix}\begin{Bmatrix} \frac{\partial u_0}{\partial x}+\frac{1}{2}\left(\frac{\partial w_0}{\partial x}\right)^2\\ \frac{\partial v_0}{\partial y}+\frac{1}{2}\left(\frac{\partial w_0}{\partial y}\right)^2\\ \frac{\partial u_0}{\partial y}+\frac{\partial v_0}{\partial x}+\frac{\partial w_0}{\partial x}\frac{\partial w_0}{\partial y}\end{Bmatrix}+\begin{bmatrix} D_{11} & D_{12} & D_{16}\\ D_{12} & D_{22} & D_{26}\\ D_{16} & D_{26} & D_{66}\end{bmatrix}\begin{Bmatrix} -\frac{\partial^2 w_0}{\partial x^2}\\ -\frac{\partial^2 w_0}{\partial y^2}\\ -2\frac{\partial^2 w_0}{\partial x\partial y}\end{Bmatrix}
\end{aligned}
\tag{3.2}
$$

where A_{ij}: extensional stiffnesses, B_{ij}: bending-extensional coupling stiffnesses, and D_{ij}: bending stiffnesses of a laminated composite plate.

In order to solve Eq. (3.1), a nonlinear finite element model is generated using conforming rectangular elements [11] with six degrees of freedom per node (Fig. 3.1) as shown in Eq. (3.3).

$$
u_0, v_0, w_0, \frac{\partial w_0}{\partial x}, \frac{\partial w_0}{\partial y}, \frac{\partial^2 w_0}{\partial x\partial y} \tag{3.3}
$$

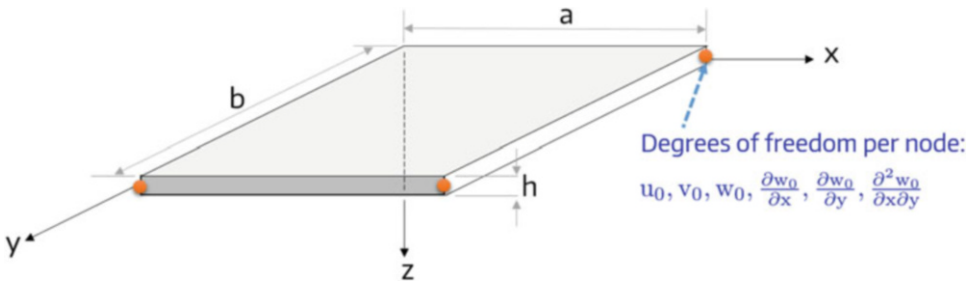

Fig. 3.1 Coordinate system and degrees of freedom per node for a conforming rectangular plate element

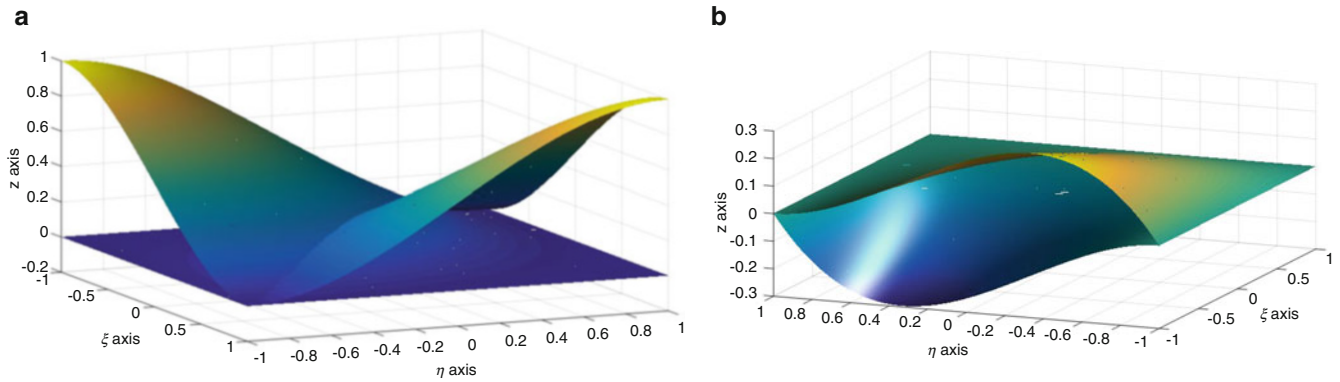

Fig. 3.2 Visualization of Hermite interpolation functions used in a conforming element with six degrees of freedom: **(a)** w_0 interpolation in the ξ-η plane, **(b)** $\partial w_0/\partial\eta$ interpolation in the ξ-η plane

These elements exhibit complete C^1-continuity, and use linear Largrange interpolation functions for u_0 and v_0, and cubic Hermite interpolation functions (Fig. 3.2) for w_0, $\frac{\partial w_0}{\partial x}$, $\frac{\partial w_0}{\partial y}$, and $\frac{\partial^2 w_0}{\partial x \partial y}$. The Hermite interpolation functions for one of the four nodes of a conforming element are described in Eq. (3.4). The complete functions can be found in [12].

$$\begin{aligned} w_0 &: \frac{1}{16}(1-\xi)^2(2+\xi)(1-\eta)^2(2+\eta) \\ \frac{\partial w_0}{\partial x} &: \frac{1}{16}(1-\xi^2)(1-\xi)(1-\eta)^2(2+\eta) \\ \frac{\partial w_0}{\partial y} &: \frac{1}{16}(1-\xi)^2(2+\xi)(1-\eta^2)(1-\eta) \\ \frac{\partial^2 w_0}{\partial x \partial y} &: \frac{1}{16}(1-\xi^2)(1-\xi)(1-\eta)^2(2+\eta) \end{aligned} \tag{3.4}$$

3.3 Experiment of Snap-Through of a Post-Buckled Thin Laminated Composite Plate

3.3.1 Digital Image Correlation (DIC) Technique

In this experiment, the digital image correlation (DIC) technique, particularly binocular stereovision technique, is used to obtain full-field measurements of the dynamic response of a plate specimen. Binocular stereovision is a technique for reconstructing a three dimensional structure from two (or more) different viewpoints of a binocular stereovision sensor which is made up of two cameras positioned in such a way that their field of view intersects [13]. As shown in the experiment setup in Fig. 3.3b, two Photron FASTCAM SA5 cameras were used as a binocular stereovison sensor which traces the random speckle pattern on the surface of the specimen (Fig. 3.3a) with 2000 Hz sampling frequency.

3.3.2 Full-Field Measurement of Nonlinear Dynamic Response

In Fig. 3.4, the top two pictures show 95 sampling points on the plate surface and four points on the clamp while the bottom two pictures are the digital images of the specimen taken by the two cameras. The left and right two images demonstrate the fields of views of the left and right cameras in Fig. 3.3b, respectively.

The rectangular laminated composite plate shown in Fig. 3.3a was used as a specimen for the dynamic test. The geometrical and material properties of the plate specimen are described in Table 3.1. The initially-flat plate was buckled and clamped. The boundary condition of the specimen for the dynamic test is clamped-clamped-free-free (CCFF); that is, the plate was clamped along the width and was free along the length. Figure 3.5a–c show the buckled shape of the specimen

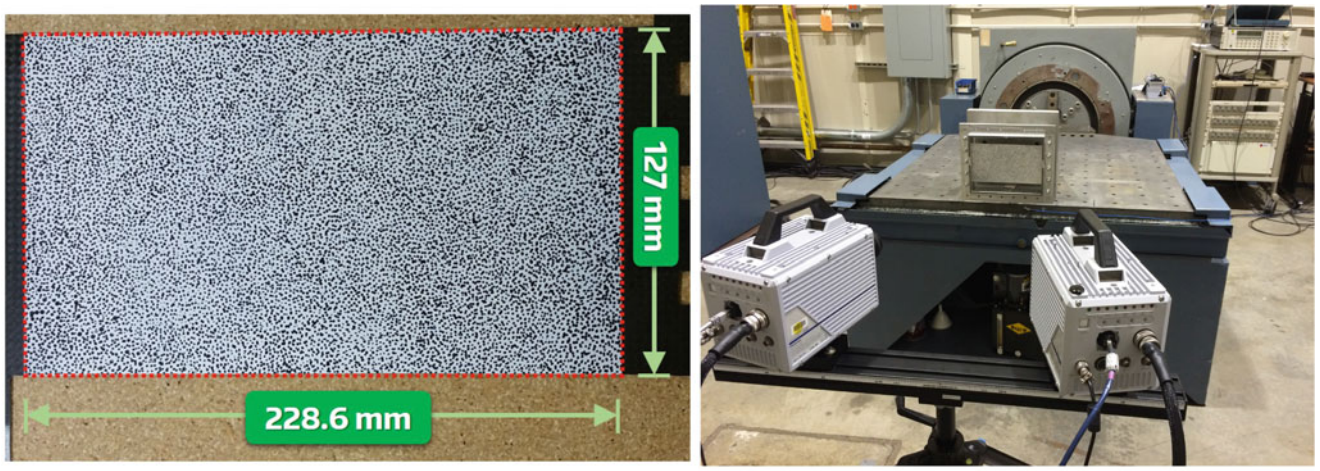

Fig. 3.3 Experiment specimen and setup. (**a**) $|45|_4$ laminated composite (plain weave) plate specimen having the dimension of 228.6 mm × 127 mm × 0.63 mm (9 in. × 5 in. × 0.025 in.) and random speckle pattern on its surface. (**b**) Dynamic experiment setup: binocular stereovision sensor (Photron FASTCAM SA5), electrodynamic shaker, and the plate specimen in (**a**) mounted in a clamp

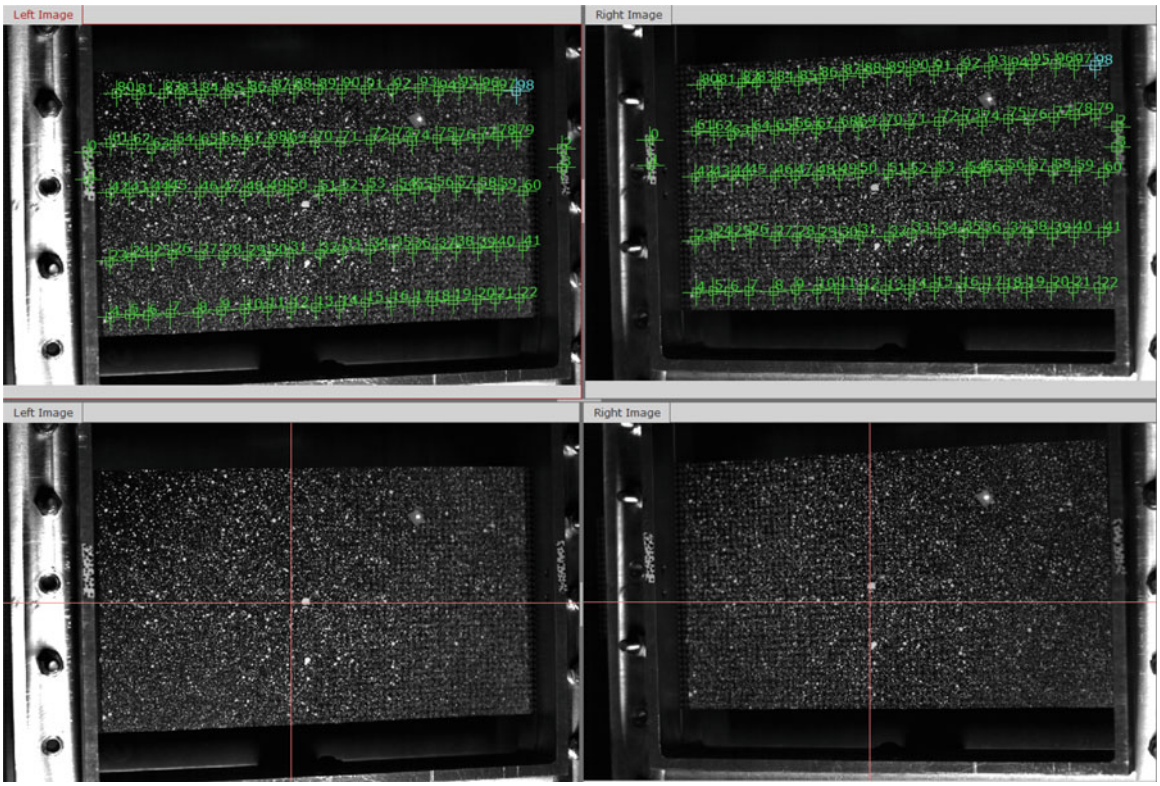

Fig. 3.4 DIC sampling points (*top pictures*) and digital images of the specimen taken by two DIC cameras (*bottom pictures*)

reconstructed by the static measurements from DIC with 13,475 sampling points before the specimen was subjected to harmonic load (at t = 0). It is observed in Fig. 3.5b, c that the buckled shape was biased along the width and length; in particular, the buckled depth (i.e., transverse displacement) at the middle of the length varied from 1.3 mm to 2.1 mm.

Figure 3.5d shows the sampling points for the DIC of the dynamic response of the specimen. There are 95 points on the plate and four points on the clamp to obtain displacements of the plate relative to the motion of the clamp. Those points were measured by the two cameras in Fig. 3.3b at 2000 Hz sampling frequency. Figure 3.6a illustrates full-field measurement of the dynamic response of the specimen subjected to 4 g harmonic load with 75 Hz forcing frequency. The 95 sampling points in Fig. 3.6a are interpolated to reconstruct the entire plate shape using MATLAB [14] and the result is shown in Fig. 3.6b. In

Table 3.1 Geometrical and material properties of specimen

Properties	Plate specimen
Prepreg	Toray T800H (plain weave)
Layup	$[45]_4$
Length, a mm (in.)	228.6 (9)
Width, b mm (in.)	127 (5)
Thickness, h mm (in.)	0.63 (0.025)
E_{11} GPa (Msi)	72.8 (10.56)
E_{22} GPa (Msi)	72.8 (10.56)
G_{12} GPa (Msi)	5.2 (0.7542)
Poisson's ratio, ν_{12}	0.3
Density, ρ kg/m^3 (lb/in.^{3})	1826 (0.0659)

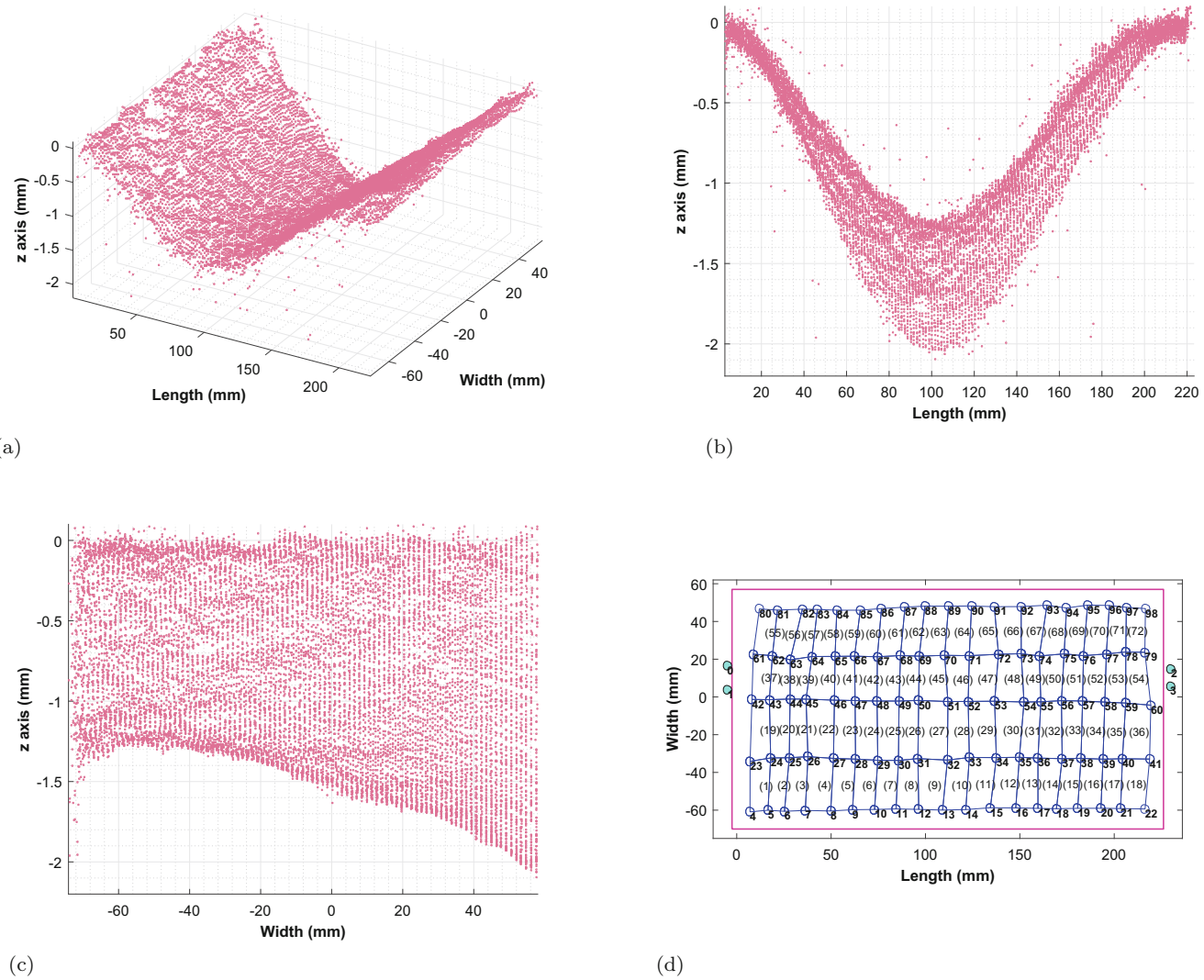

Fig. 3.5 DIC of static and dynamic measurement. (**a**) Buckled shape of the specimen reconstructed by the static measurements from DIC with 13,475 sampling points. (**b**) Buckled shape of the specimen along the length. (**c**) Buckled shape of the specimen along the width. (**d**) Superposition of the specimen plate (*pink line*), 95 sampling points on the plate (*blue empty circles*), and four sampling points on the clamp (*cyan-filled circles*) for dynamic DIC measurement

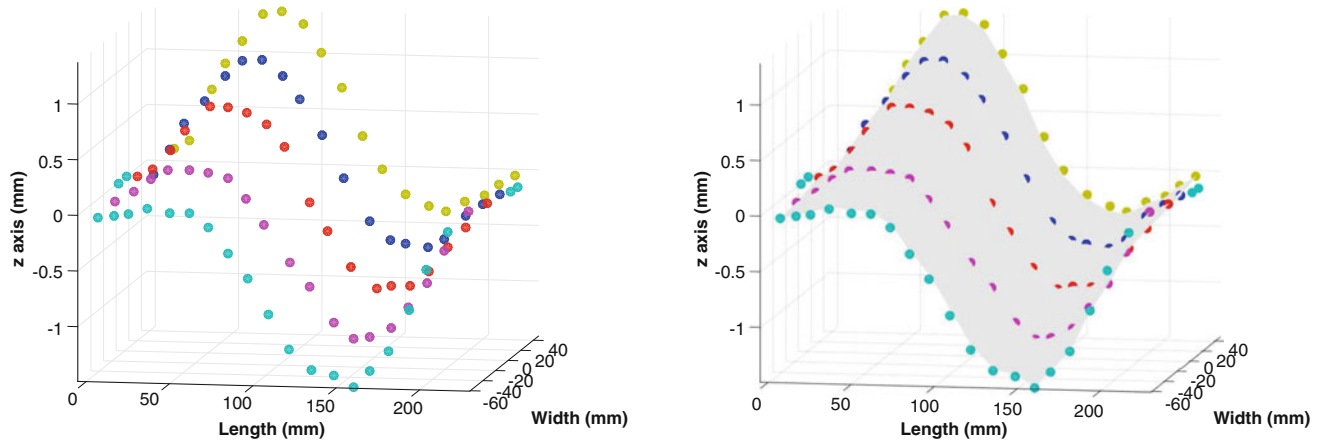

Fig. 3.6 Full-filed measurement of the dynamic response of the specimen. (**a**) Full-filed measurement of the dynamic response of the specimen subjected harmonic loading. (**b**) Interpolated deflected shape using the 95 sampling points in (**a**)

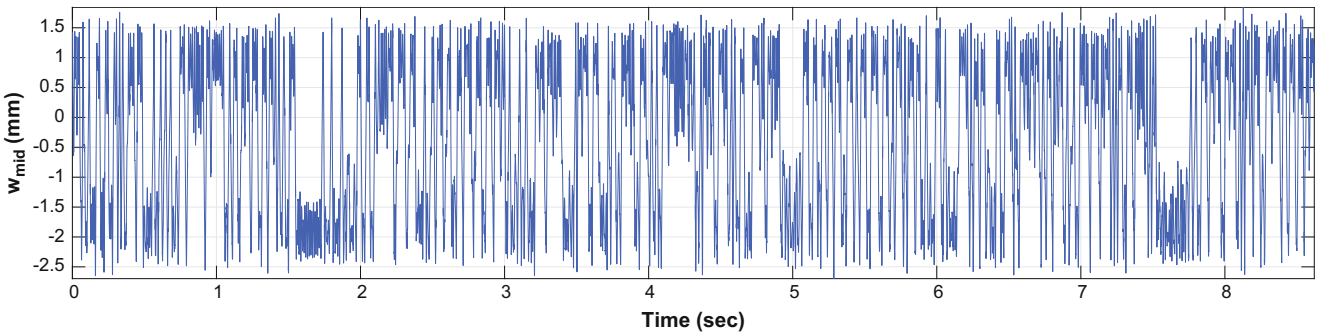

Fig. 3.7 Transverse response of the midpoint of the specimen (sampling point number 51 in Fig. 3.5d)

that figure, it is observed that the non-uniform buckled shape affected the dynamic response such that the fifth row of circles (olive-colored circles) in Fig. 3.6a which had the deepest buckled depth ($\simeq$ 2.1 mm) in Fig. 3.5c is located at the highest while the first row (cyan-colored circles) which had the shallowest buckled depth ($\simeq$ 1.3 mm) is positioned at the lowest.

The sampling point number 51 in Fig. 3.5d whose initial buckled depth in Fig. 3.5a is 1.3896 mm was chosen as the (nominal) midpoint of the plate. Figure 3.7 shows the transverse response of the midpoint (w_{mid}) for 8.62 s. In the plot, it is observed that the post-buckled plate demonstrated chaotic (intermittent) snap-through under the 4 g harmonic load with 75 Hz forcing frequency. The midpoint recurrently oscillated around one of its stable equilibria and then snapped into the other stable equilibrium point in a chaotic manner. When it oscillated around a stable equilibrium point, the peak-to-peak response was approximately 0.8 mm; however, the peak-to-peak displacement during the snap-through was around 4.1 mm, a significant increase compared to the single-well response.

Figure 3.8 is the state-space of the midpoint of the specimen. The sampling frequency was too low to capture smooth curves in the state-space. Considering the plots of the state-space and of the transverse response in Fig. 3.7, the separatrix (basin boundary) [15] of the transverse dynamic response of the midpoint (w_{mid}) appears to be located (nominally) at between $w_{mid} = -0.5$ and -1.0 mm. Since the separatrix is higher-dimensional, the discussion on the separatrix in this section relates to its dimension of the plate midpoint displacement (w_{mid}). It is also observed that the upper equilibrium point ($w_{mid} \simeq 1.0$ mm) is closer to the neutral point ($w_{mid} = 0$ mm) than is the lower equilibrium point ($w_{mid} \simeq -2.0$ mm).

Figure 3.9 demonstrates a part of the chaotic transverse response in Fig. 3.7 for 0.45 s and the corresponding interpolated deflected shapes of the plate. At the peak point (1), the plate in Fig. 3.9b oscillated around the upper equilibrium point and the first mode was dominating the response. When the plate approached the assumed separatrix ($w_{mid} \simeq -0.5$ mm ~ -1.0 mm) at (2), the dominance of the second mode is observed in Fig. 3.9c. The plate could not snap into the lower equilibrium point at (2) and continued to oscillate around the upper equilibrium point. The plate at (3) (Fig. 3.9d) showed a bigger displacement at the peak than did the one at (1) and snapped into the lower equilibrium point to arrive at the other peak at (5) (Fig. 3.9f). When the plate passed the assumed separatrix of w_{mid} at (4) (Fig. 3.9e), it is observed that the response amplitude was

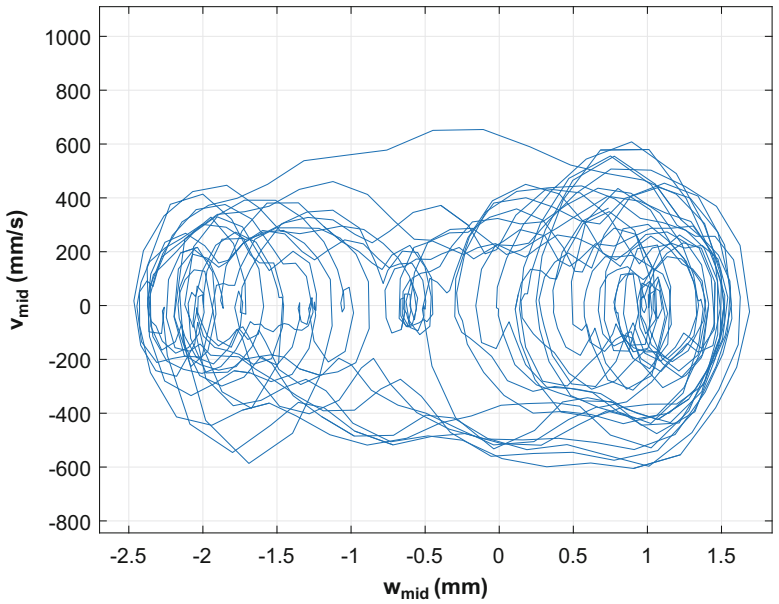

Fig. 3.8 State-space of the midpoint of the specimen

significantly smaller than the amplitude at (2) and that the plate looked almost flat. This is an interesting phenomenon since plates experience large amplitude compressive load when they pass their neutral points where $w_{mid} = 0$ and thus the plates typically demonstrate dominance of higher modes. The plate at (6) (Fig. 3.9g) had a response amplitude slightly smaller than did the one at (3). Although the plate moved into the immediate vicinity of the assumed saparatrix at (7) (Fig. 3.9h), it could not snap into the other equilibrium point and continued to oscillate the upper equilibrium point.

3.4 Modeling of Snap-Through of a Post-Buckled Thin Laminated Composite Plate

3.4.1 Static Analysis

A nonlinear finite element model, based on Eqs. (3.1) and (3.2), conforming elements, and Hermite interpolation functions, was generated using MATLAB [14]. The static equilibrium path of the initially-flat specimen subjected to axial loading was analyzed using the mesh in Fig. 3.10a which has 231 nodes and 200 elements, and the results are shown in Fig. 3.10b. In the plot, the loading parameter $\lambda = 1$ is equal to the axial load for the first buckling mode, 695.5 N/m.

In the static DIC measurement of the initial post-buckled specimen shown in Sect. 3.3.2, it was observed that the buckled depth at the middle of the length of the specimen varies from 1.3 to 2.1 mm (Fig. 3.5). Considering the variance of the buckled depth, two different cases are analyzed: two plates with 1 and 2 mm-buckled at the midpoint, respectively. The equilibrium paths of these post-buckled plate were analyzed using the linearized arc-length method [16, 17] and the branch switching technique [18, 19]. The results are illustrated in Figs. 3.11 and 3.12, and are summarized in Table 3.2.

Figure 3.11 demonstrates the equilibrium path and corresponding deflected shapes of the 1 mm-buckled plate case. In the plot, the loading parameter $\lambda = 1$ is equal to a concentrated load P = 0.01 N at the midpoint of the plate (Node 116 in Fig. 3.10a). As shown in Fig. 3.11b, the midpoint of the plate had -1.0024 mm-initial transverse displacement (buckled depth) at (1). In Fig. 3.11c, the midpoint arrived at its first limit point (2) and followed its unstable primary equilibrium path at $\lambda = 93.546$ (i.e., P = 0.935 N). Using the branch-switching process, the bifurcation of the post-buckled plate into the unstable secondary path and increase in influence of the second mode occurred at (3) after the midpoint passed its first limit point (2). This phenomenon typically happens for arches of intermediate rise. As shown in Fig. 3.11d, after the bifurcation at (3), the difference between the transverse displacement of the one-quarter point ($w_{1/4}$) of the length (Node 61) and the three-quarter point ($w_{3/4}$) of the length (Node 171) increased until the midpoint arrived at the neutral point (4) in Fig. 3.11f where $w_{mid} = 0$ and $w_{\frac{1}{4}} - w_{\frac{3}{4}}$ reached its maximum value, 0.0445 mm. This phenomenon demonstrates the dominance of the second mode between the first bifurcation and neutral points along the secondary path. The plate returned to the unstable

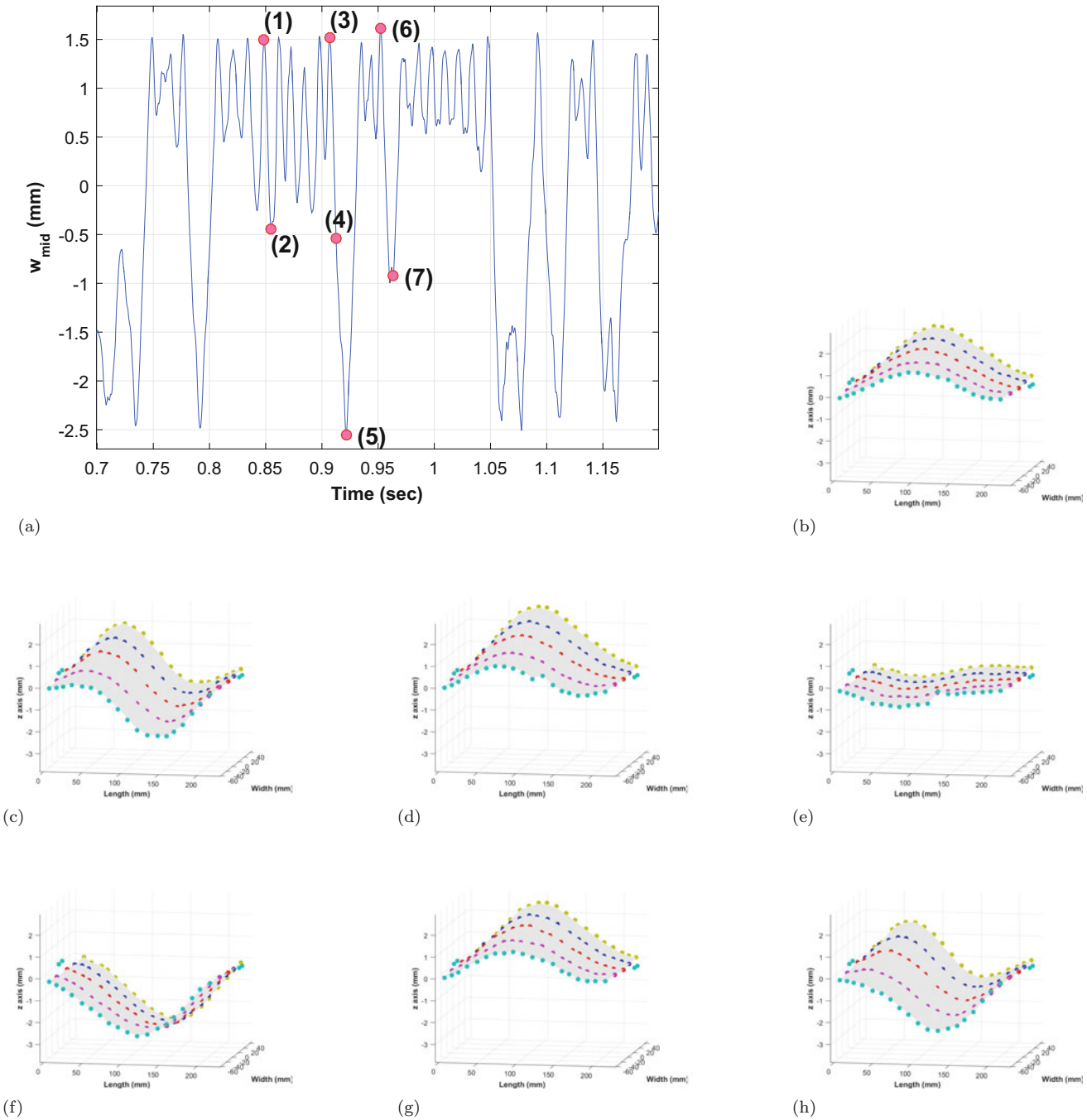

Fig. 3.9 Chaotic dynamic response of the midpoint and corresponding interpolated deflected shapes of the specimen. (**a**) Part of the chaotic transverse response of the midpoint of the specimen in Fig. 3.7. (**b**) Interpolated deflected shape at (1). (**c**) Interpolated deflected shape at (2). (**d**) Interpolated deflected shape at (3). (**e**) Interpolated deflected shape at (4). (**f**) Interpolated deflected shape at (5). (**g**) Interpolated deflected shape at (6). (**h**) Interpolated deflected shape at (7)

primary path at the second bifurcation point (5). Finally, at the second limit point (6), the midpoint began to followed the stable primary path again.

Figure 3.12 demonstrates the equilibrium path and corresponding deflected shapes of the 2 mm-buckled plate case. As shown in Fig. 3.12b, the midpoint of the plate had −2.0023 mm-initial transverse displacement (buckled depth) at (1). In Fig. 3.12c, the middle point arrived at its first bifurcation point (2) and the branch-switching process helped the plate bifurcate into the unstable secondary equilibrium path at $\lambda = 451.828$ (i.e., P = 4.518 N). In contrast to the 1 mm-buckled plate case (an arch of intermediate rise), the 2 mm-buckled plate (a deep arch) bifurcated before the midpoint of the plate passed its

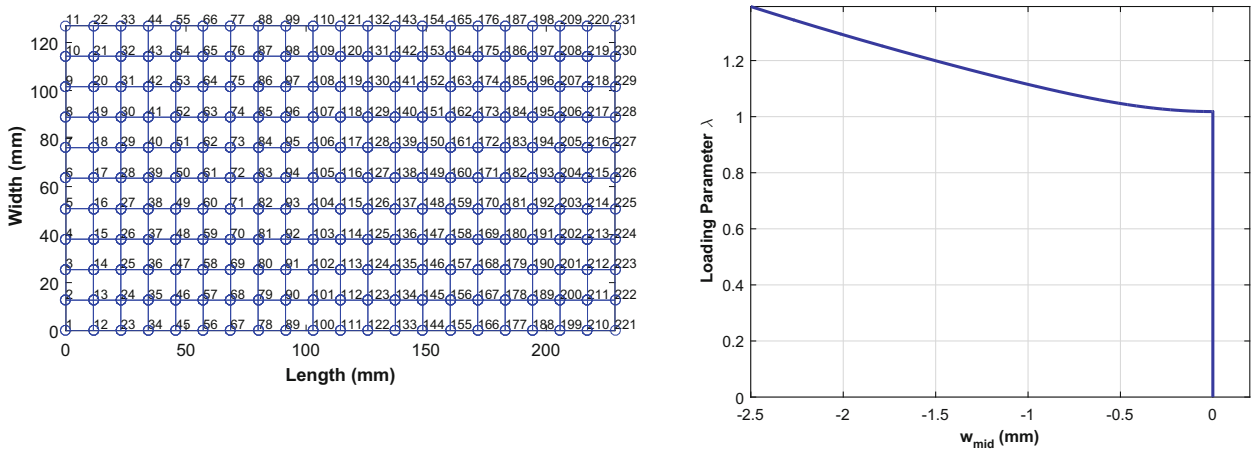

(a) (b)

Fig. 3.10 FEM mesh and equilibrium path of the initially-flat plate specimen subjected to axial loading. (**a**) FEM mesh with 231 nodes and 200 elements. (**b**) Equilibrium path of the initially-flat plate specimen under axial loading

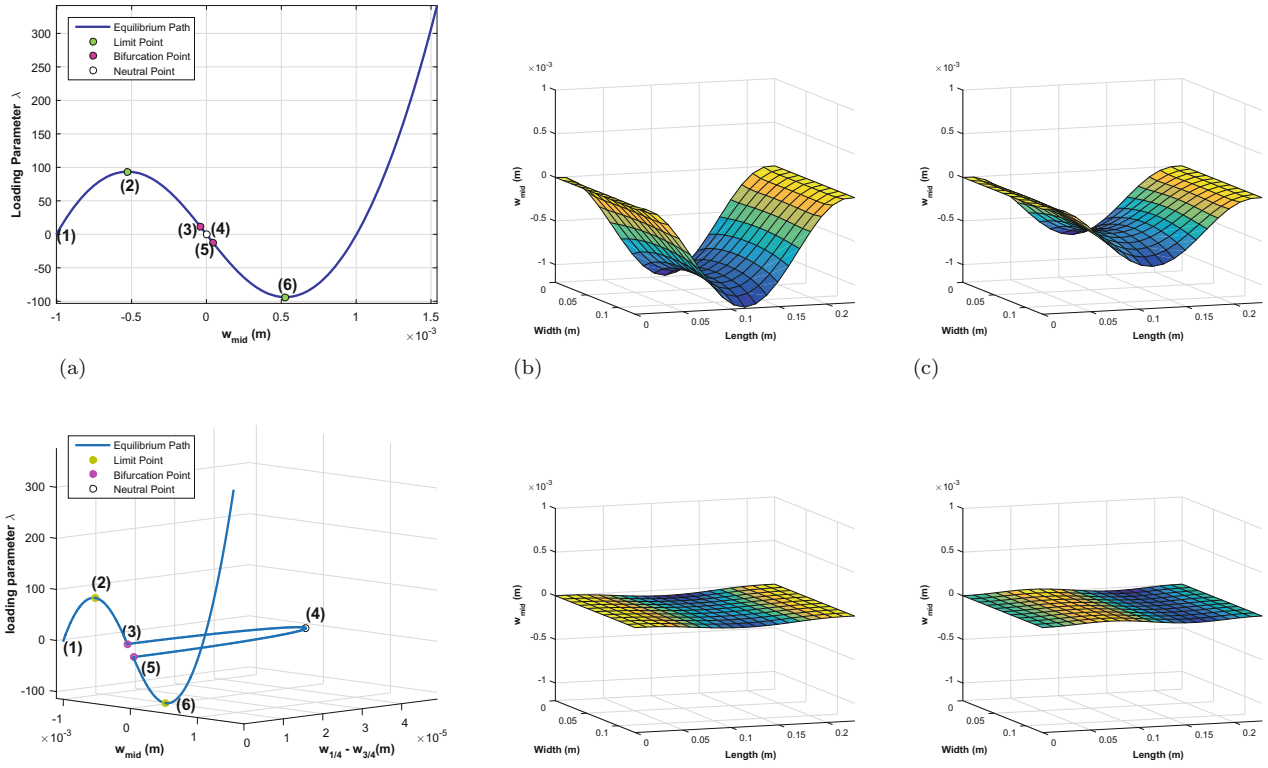

(a) (b) (c) (d) (e) (f)

Fig. 3.11 Equilibrium path and corresponding deflected shapes of the post-buckled plate (1 mm). (**a**) 2D Equilibrium path (w_{mid} vs. λ). (**b**) Deflected shape at the initial state. (**c**) Deflected shape at the first limit point (2). (**d**) 3D Equilibrium path (w_{mid} vs. $w_{\frac{1}{4}} - w_{\frac{3}{4}}$ vs. λ). (**e**) Deflected shape at the first bifurcation point. (**f**) Deflected shape at the neutral point (4)

first limit point. As shown in Fig. 3.12d, after the bifurcation at (2), the difference between the transverse displacement of the one-quarter point ($w_{1/4}$) of the length at Node 61 and the three-quarter point ($w_{3/4}$) of the length at Node 171 increased until the midpoint arrived at the neutral point (3) in Fig. 3.12d where $w_{mid} = 0$ and $w_{\frac{1}{4}} - w_{\frac{3}{4}}$ reached its maximum value, 1.4944 mm. This case illustrates the dominance of the second mode between the first bifurcation and neutral points along the secondary path. The plate returned to the stable primary path at the second bifurcation point (4) and the midpoint continued to follow the stable primary path again.

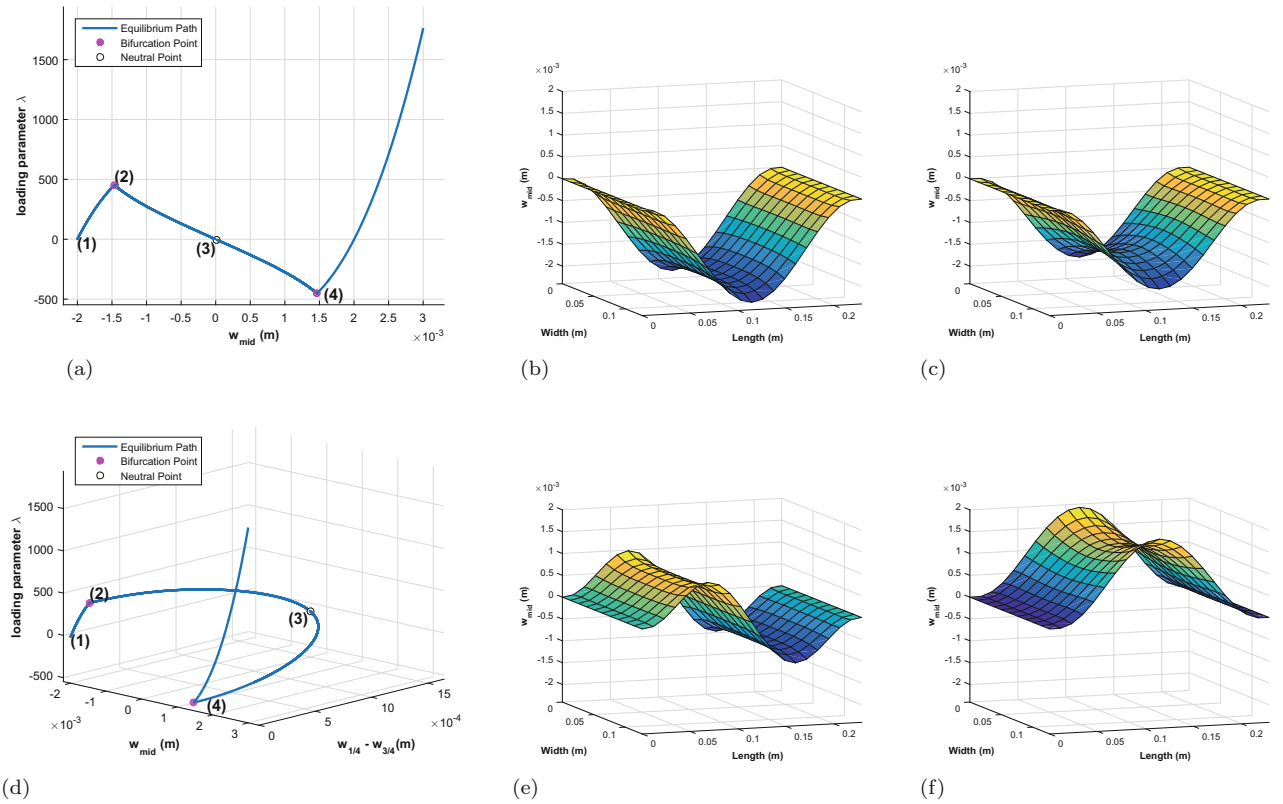

Fig. 3.12 Equilibrium path and corresponding deflected shapes of the post-buckled plate (2 mm). (**a**) 2D Equilibrium path (w_{mid} vs. λ). (**b**) Deflected shape at the initial state. (**c**) Deflected shape at the first bifurcation point (2). (**d**) 3D Equilibrium path (w_{mid} vs. $w_{\frac{1}{4}} - w_{\frac{3}{4}}$ vs. λ). (**e**) Deflected shape at the neutral point (3). (**f**) Deflected shape at the second bifurcation point (4)

Table 3.2 Limit and bifurcation points of 1 mm- and 2 mm-buckled plates

Point	Values	1 mm buckled	2 mm buckled
Initial	w_{mid} (mm)	−1.0024	−2.0023
	λ	0	0
First limit	w_{mid} (mm)	−0.5269	N/A
	λ	93.5463	N/A
First bifurcation	w_{mid} (mm)	−0.04234	−1.4654
	λ	11.9500	451.8278
Neutral	w_{mid} (mm)	0.0005	0.0160
	$w_{\frac{1}{4}} - w_{\frac{3}{4}}$	0.0445	1.4944
	λ	−0.2489	−4.2111
Second bifurcation	w_{mid} (mm)	0.04235	1.4654
	λ	−12.1530	−452.0284
Second limit	w_{mid} (mm)	0.5269	N/A
	λ	−93.7463	N/A

Where the loading parameter $\lambda = 1$ is equals to the concentrated load $P = 0.01$ N at Node 116 in Fig. 3.10a

3.4.2 Dynamic Analysis

The dynamic response of the post-buckled plate is modeled using MATLAB [14]. The direct time integration, in particular implicit Newmark method [20] was applied to the nonlinear finite element model and mesh used in Sect. 3.4.1. Using this method, the expression of velocity and displacement vectors of the system, $\dot{u}_{n+1}$ and u_{n+1} respectively, can be written as:

$$\begin{aligned} \dot{u}_{n+1} &= \dot{u}_n + (1-\gamma)\Delta t\ddot{u}_n + \gamma\Delta\ddot{u}_{n+1} \\ u_{n+1} &= u_n + \Delta t\dot{u}_n + \left(\frac{1}{2} - \beta\right)\Delta t^2\ddot{u}_n + \beta\Delta t^2\ddot{u}_{n+1} \end{aligned} \tag{3.5}$$

$\gamma = \frac{1}{2}$ and $\beta = \frac{1}{4}$ (i.e., average acceleration method or trapezoidal rule) were chosen for the above equation to be unconditionally stable [21]. In addition, in this dynamic model, the damping effect was not considered.

Since the midpoint of the specimen used in the plot in Fig. 3.7 had an initial displacement, −1.3896 mm, a plate with a midpoint (Node 116 in Fig. 3.10a) with the same buckled depth was used for the dynamic analysis of the post-buckled plate. Since asymmetric deflected shapes were observed in the vicinity of the neutral point during snap-through in the experimental results, an small imperfection, to induce asymmetric deflected shapes, was embedded in the initial buckled shape of the plate using the second mode whose $w_{1/4} = w_{3/4} = 1 \times 10^{-6}$ mm.

A dynamic analysis result of the transverse response of the midpoint (w_{mid}) subjected to 4 g harmonic load with 75 Hz forcing frequency are illustrated in Fig. 3.13. While the response of the experiment under the same load exhibited chaotic snap-through response in Fig. 3.7, the modeling result showed a single-well response where the midpoint of the plate oscillated between −1.1262 and −1.6352 mm and could not snap into the other equilibrium point. As demonstrated in the corresponding deflected shapes, the dominance of the first mode was conspicuous under this loading amplitude.

The forcing amplitude of the model was gradually amplified to find a chaotic snap-through boundary and when the amplitude reached 8 g, response from the model demonstrated chaotic snap-through as shown in Fig. 3.14. When the plate passed the neutral point ($w_{mid} = 0$) at (3), (4), and (5), the plate exhibited different deflected shapes illustrated in Fig. 3.14d–f, respectively. The plate showed an asymmetric deflected shape at (4) where $w_{3/4}$ was higher than $w_{1/4}$; in contrast, $w_{1/4}$ of the deflected shape at (5) was higher than its $w_{3/4}$. The deflected shape of (3) appeared to be flat and this phenomenon was also observed in the experiment (Fig. 3.9d). Figure 3.14g indicates the influence of the third mode on the deflected shape.

The forcing amplitude of the model was increased further to find a periodic snap-through boundary and when the amplitude approached 10g, periodic snap-through was observed from the dynamic analysis of the model (Fig. 3.15). The midpoint persistently snapped into one of the two stable equilibria. Similar to the chaotic case, the periodic snap-through case also exhibited flat and asymmetric deflected shapes when the plate approached the neutral point.

3.5 Comparison of Modeling and Experimental Results

The snap-through response of the midpoint obtained from the experiment (Fig. 3.7) and from the model (Fig. 3.14a) exhibited similar peak-to-peak displacements, approximately 4.2 mm. In addition, both demonstrated similar flat (Figs. 3.9e and 3.14d) and asymmetric deflected shapes (Figs. 3.9c, 3.9h, 3.14e, and 3.14f) in the vicinity of the neutral point.

However, while the test specimen subjected to 4 g harmonic load with 75 Hz forcing frequency exhibited chaotic snap-through response (Fig. 3.7), the analysis result from the numerical model demonstrated a single-well response under the same load (Fig. 3.13). In addition, the model predicted that the chaotic snap-through boundary in the harmonic forcing parameter space is 8 g at 75 Hz although the test specimen exhibited chaotic snap-through below that boundary. That discrepancy may have been attributable to the non-uniform buckled shape illustrated in Fig. 3.5. Since the plate specimen in the experiment had a non-uniform buckled shape while the buckled plate used in the modeling had a uniform buckled depth along its length, the two plates likely have different natural frequencies and consequently different snap-through boundaries. A schematic figure of presumed snap-through boundaries of the plates are illustrated in Fig. 3.16. Although some parts of the test specimen had deeper buckled-depth, in case the natural frequency of the specimen is higher than the natural frequency of the modeled plate as demonstrated in the schematic figure, chaotic snap-through of the specimen could be initiated with smaller forcing amplitude.

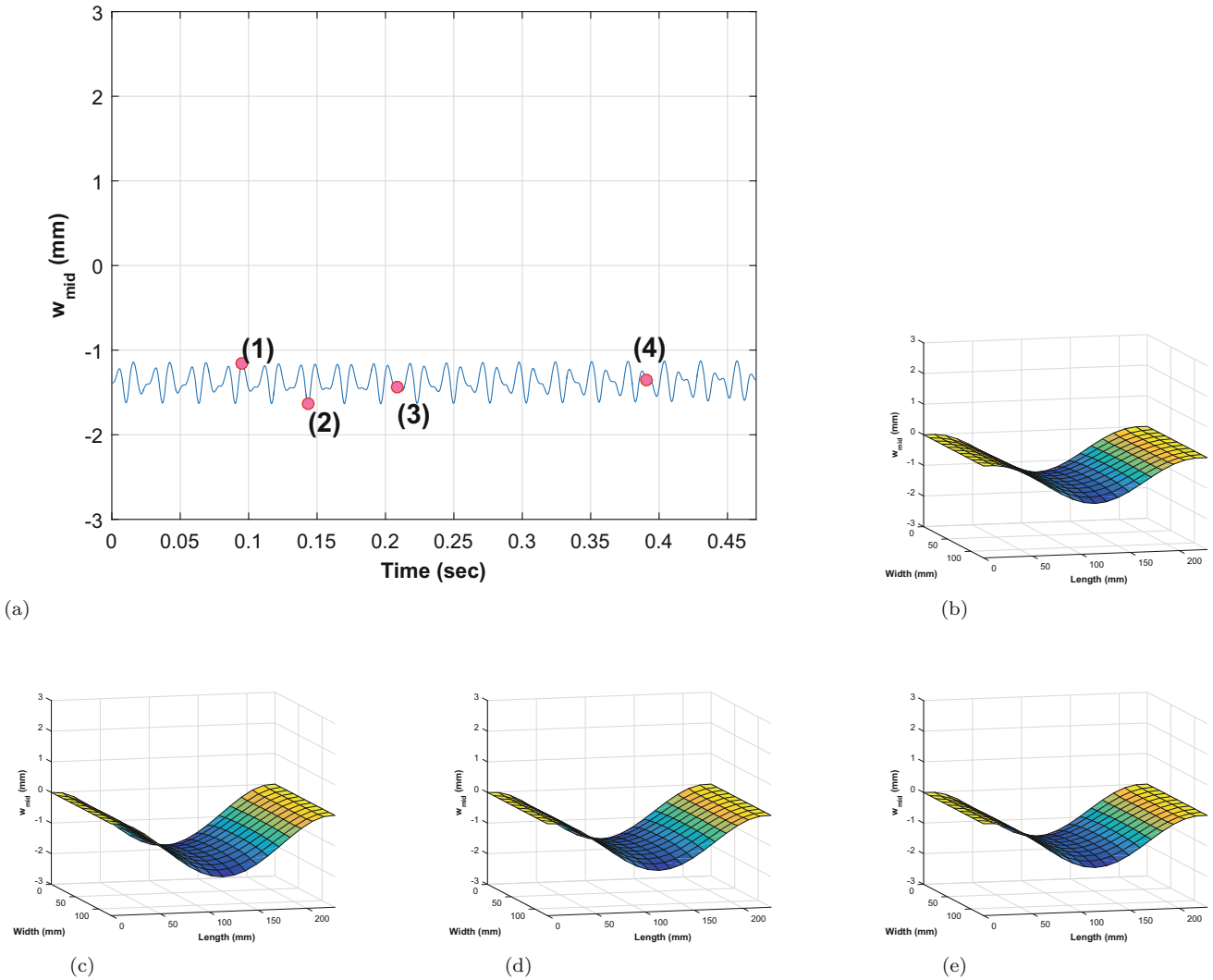

Fig. 3.13 Transverse response of the midpoint subjected to 4 g harmonic load with 75 Hz forcing frequency and corresponding deflected shapes. (**a**) Transverse response of the midpoint subjected to 4 g harmonic load with 75 Hz forcing frequency [w_{mid} vs. Time (s)]. (**b**) Deflected shape at (1). (**c**) Deflected shape at (2). (**d**) Deflected shape at (3). (**e**) Deflected shape at (4)

3.6 Summary and Future Work

The experimental data of dynamic response of a post-buckled thin composite plate was collected using the digital image correlation (DIC) technique and was presented in this paper. Dynamic response of a post-buckled plate were numerically analyzed using a nonlinear finite element model and snap-through boundaries of the plate were illustrated with the modeling results.

Although both the experiments and the numerical analysis demonstrated similar patterns of chaotic snap-through response, it was observed that the chaotic snap-through boundary predicted by the model is located higher at the applied forcing frequency in the harmonic forcing parameter space than is the boundary of the test specimen. This discrepancy will be more examined by modeling a post-buckled plate to have the same nonuniform buckled shape as the test specimen.

In future work, the nonlinear dynamic behavior and snap-through of post-buckled composite plates will be further investigated. Of particular interest will be in-plane compressive loading induced by snap-through and its potential for causing delaminations.

Acknowledgements The authors wish to thank Stephen M. Spottswood for granting access to the Air Force Research Laboratory equipment, and David Ehrhardt, Michelle Hickner, Bill Kuykendall, and Minyong Lee for their assistance in the laboratory.

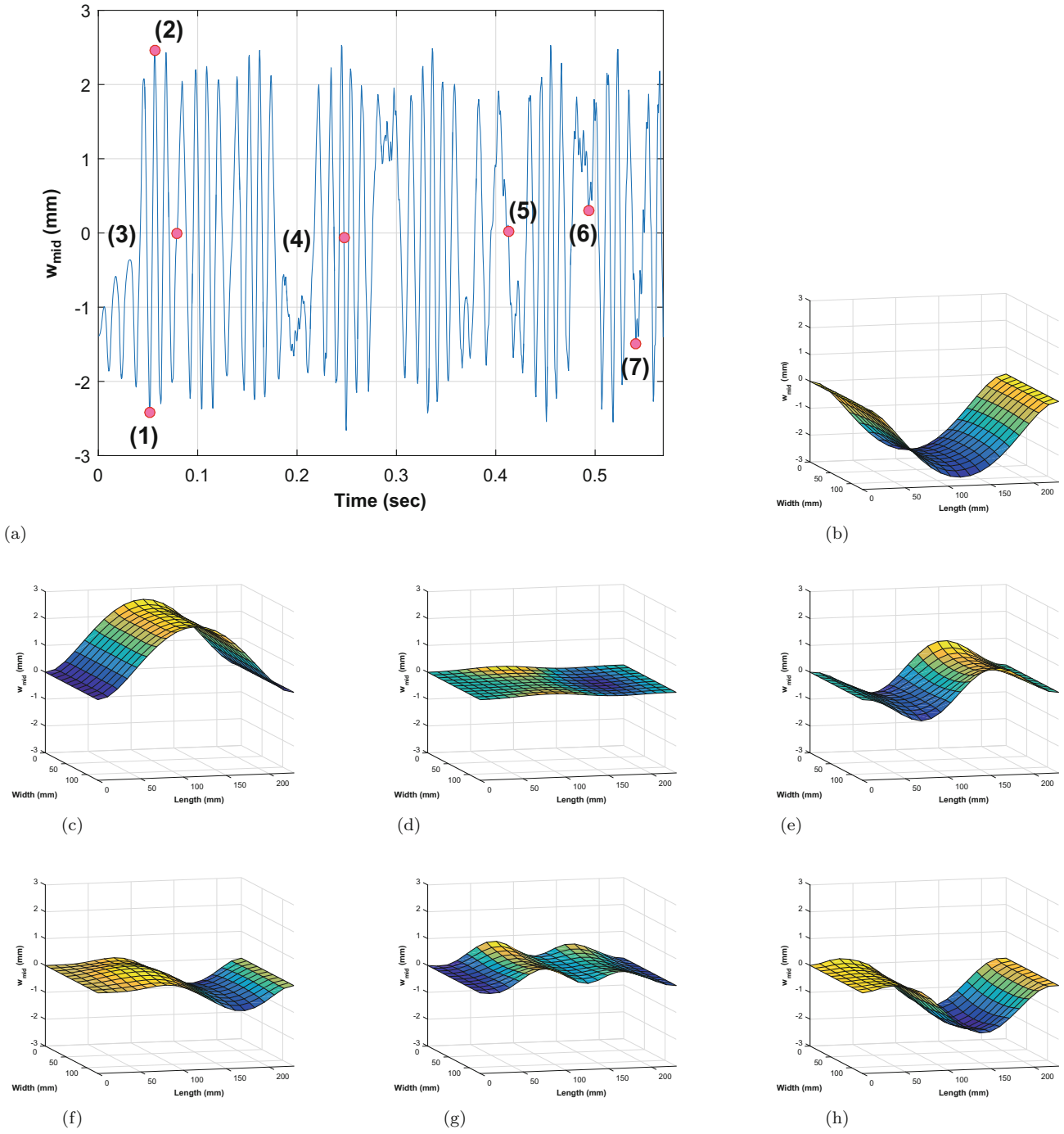

Fig. 3.14 Transverse response of the midpoint subjected to 8 g harmonic load with 75 Hz forcing frequency and corresponding deflected shapes. (**a**) Transverse response of the midpoint subjected to 8 g harmonic load with 75 Hz forcing frequency [w_{mid} vs. Time (s)] ((3) and (4) are intentionally written away from their points not to obstruct the plot). (**b**) Deflected shape at (1). (**c**) Deflected shape at (2). (**d**) Deflected shape at (3), 0.0790 s. (**e**) Deflected shape at (4), 0.2471 s. (**f**) Deflected shape at (5). (**g**) Deflected shape at (6). (**h**) Deflected shape at (7)

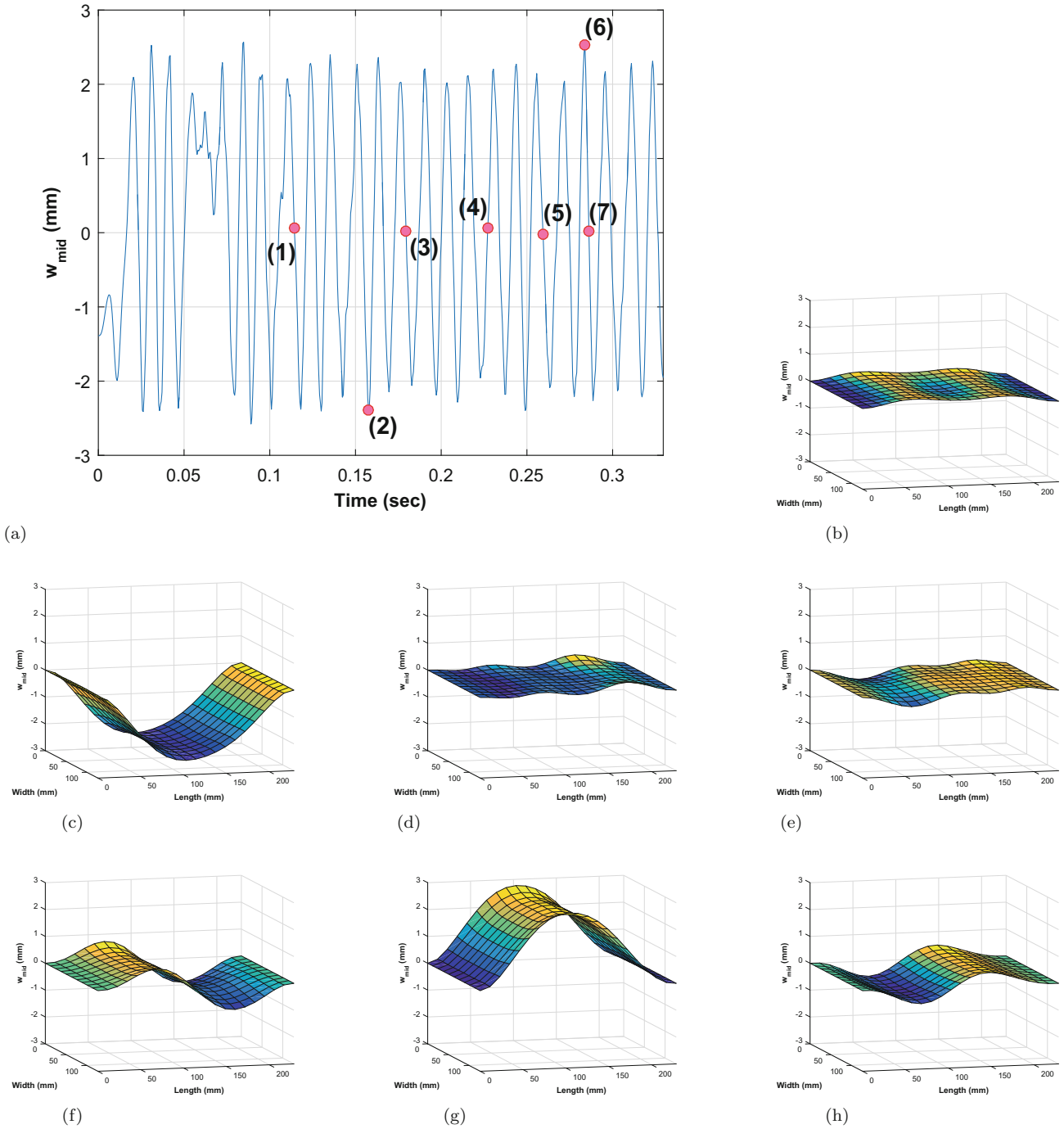

Fig. 3.15 Transverse response of the midpoint subjected to 10g harmonic load with 75 Hz forcing frequency and corresponding deflected shapes. (**a**) Transverse response of the midpoint subjected to 10g harmonic load with 75 Hz forcing frequency [w_{mid} vs. Time (s)]. (**b**) Deflected shape at (1). (**c**) Deflected shape at (2). (**d**) Deflected shape at (3), 0.0790 s. (**e**) Deflected shape at (4), 0.2471 s. (**f**) Deflected shape at (5). (**g**) Deflected shape at (6). (**h**) Deflected shape at (7)

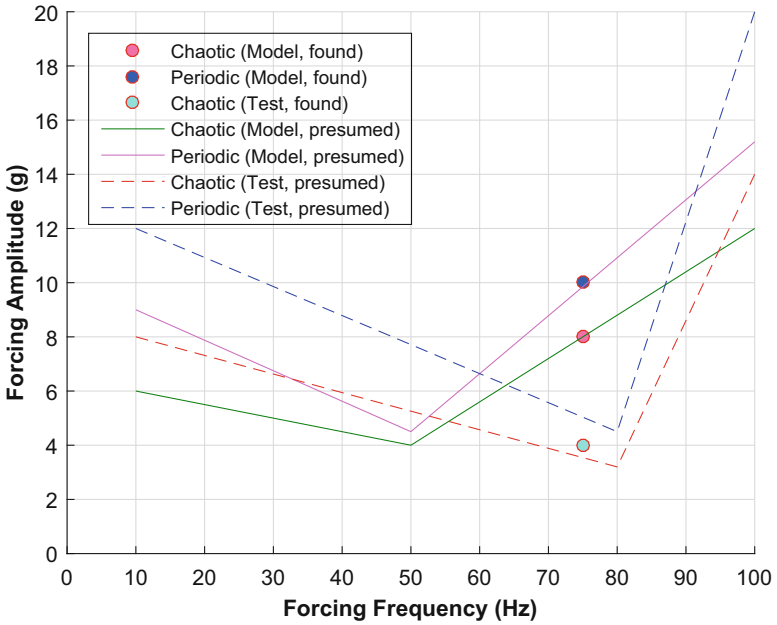

Fig. 3.16 A schematic figure of presumed snap-through boundaries of the buckled plates used in the experiment and the modeling in the harmonic forcing parameter space. This figure is purely schematic away from 75 Hz, and shows a possible explanation of the discrepancy between the experimental and modeling results

References

1. Khandan, R., Noroozi, S., Sewell, P., Vinney, J.: The development of laminated composite plate theories: a review. J. Mater. Sci. **47**, 5901–5910 (2012)
2. Gibson, R.F.: Principles of Composite Material Mechanics. CRC, Boca Raton, FL (2012)
3. Chai, H., Babcock, C.D., Knauss, W.G.: Thermal buckling analysis of rectangular panels subjected to humped temperature profile heating. NASA/TP-2004-212041 (2004)
4. Murphy, K.D., Ferreira, D.: Thermal buckling of rectangular plates. Int. J. Solids Struct. **38**, 3979–3994 (2001)
5. Chai, H., Babcock, C.D., Knauss, W.G.: One dimensiona modelling of failure in laminated plates by delamination buckling. Int. J. Solids Struct. **17**(11), 1069–1083 (1981)
6. Chai, H., Babcock, C.D., Knauss, W.G.: Vibration-based model-dependent damage delamination identification and health monitoring for composite structures - a review. J. Sound Vib. **230**(2), 357–378 (2000)
7. Murphy, K.D., Virgin, L.N., Rizzi, S.A.: Experimental snap-through boundaries for acoustically excited thermally buckled plates. Exp. Mech. **36**, 312–317 (1996)
8. Przekop, A.K., Rizzi, S., Sweitzer, K.: An investigation of high-cycle fatigue models for metallic structures exhibiting snap-through response. Int. J. Fatigue **30**, 1579–1598 (2008)
9. Reddy, J.N.: Mechanics of Laminated Composite Plates and Shells. CRC, Boca Raton, FL (2004)
10. Reddy, J.N.: Theory and Analysis of Elastic Plates and Shells. CRC, Boca Raton, FL (2007)
11. Bogner, F.K., Fox, R.L., Schmidt, Jr.L.A.: The generation of inter-element-compatible stiffness and mass matrices by the use of interpolation formulas. J. Sound Vib. **31**(3), 257–293 (1973)
12. Dhatt, G., Touzot, G., Lefrancois, E.: Finite Element Method. Wiley, New York (2012)
13. Grediac, M., Hild, F.: Full-Field Measurements and Identification in Solid Mechanics. Wiley, New York (2012)
14. MATLAB R2015b. The MathWorks (2015)
15. Strogatz, S.H.: Nonlinear Dynamics and Chaos. Westview, Cambridge, MA (2015)
16. Schweizerhof, K.H., Wriggers, P.: Consistent linearization for path following methods in nonlinear fe analysis. Comput. Methods Appl. Mech. Eng. **59**, 261–279 (1986)
17. Crisfield, M.A.: Non-linear Finite Element Analysis of Solids and Structures, Volume 1: Essentials. Wiley, New York (1991)
18. Crisfield, M.A.: Non-linear Finite Element Analysis of Solids and Structures, Volume 2: Advanced Topics. Wiley, New York (1997)
19. Shi, J., Crisfield, M.A.: A semi-direct approach for the computation of singular points. Comput. Struct. **51**(1), 107–115 (1994)
20. Newmark, N.M.: A method of computation for structural dynamics. J. Eng. Mech. Div. **85**, 67–94 (1959)
21. Paultre, P.: Dynamics of Structures. Wiley, New York (1991)